

SCIENTIFIC REPORTS



OPEN

Optimization of self-catalyzed InAs Nanowires on flexible graphite for photovoltaic infrared photodetectors

Received: 08 December 2016

Accepted: 08 March 2017

Published: 10 April 2017

Ezekiel A. Anyebe^{1,†}, I. Sandall², Z. M. Jin¹, Ana M. Sanchez³, Mohana K. Rajpalke⁴, Timothy D. Veal⁴, Y. C. Cao⁵, H. D. Li⁶, R. Harvey¹ & Q. D. Zhuang¹

The recent discovery of flexible graphene monolayers has triggered extensive research interest for the development of III-V/graphene functional hybrid heterostructures. In order to fully exploit their enormous potential in device applications, it is essential to optimize epitaxial growth for the precise control of nanowire geometry and density. Herein, we present a comprehensive growth study of InAs nanowires on graphitic substrates by molecular beam epitaxy. Vertically well-aligned and thin InAs nanowires with high yield were obtained in a narrow growth temperature window of 420–450 °C within a restricted domain of growth rate and V/III flux ratio. The graphitic substrates enable high nanowire growth rates, which is favourable for cost-effective device fabrication. A relatively low density of defects was observed. We have also demonstrated InAs-NWs/graphite heterojunction devices exhibiting rectifying behaviour. Room temperature photovoltaic response with a cut-off wavelength of 3.4 μm was demonstrated. This elucidates a promising route towards the monolithic integration of InAs nanowires with graphite for flexible and functional hybrid devices.

Semiconductor nanowires (NWs) have emerged as potentially important building blocks for future photonic and electronic devices due to their unique properties including superior light absorption, enhanced photo-carrier separation and epitaxial growth insensitive to lattice mismatch¹. Particularly, InAs NWs are highly promising for applications in high-speed electronics and mid-infrared optoelectronic devices owing to their narrow direct band gap (0.35 eV), small electron effective mass and high electron mobility (~30,000 cm²/Vs at 300 K)^{2–4}. Graphene/graphitic films on the other hand exhibit excellent electrical and thermal conductivity, high mechanical robustness, superb transparency, mechanical flexibility and unique optical properties⁵ which has made them an ideal transparent conducting electrode to replace conventional indium tin oxide (ITO)^{6,7}. The monolithic integration of semiconductor NWs with graphene/graphitic substrates (GS) has stimulated enormous research interest over recent years as it would enable the exploitation of these exceptional material properties. Together with the scalability^{8,9} and relative abundance of graphene, this technology provides a unique platform for the development of high performance, flexible and cost-effective optoelectronic nanodevices, such as flexible displays, printable electronics, sensors, light emitting diodes and flexible solar cells^{10–12}. Several devices have recently been demonstrated including hybrid graphene/ZnO NWs¹¹ and graphene/n-Si Schottky junction¹³ solar cells and light emitting diodes¹⁴.

In contrast to conventional semiconductor substrates which possess covalent bonding, GS lacks surface dangling bonds which makes them chemically inert to foreign atoms. As a result NWs growth on GS is very challenging⁵. The small bond length of the graphene lattice¹⁵ (1.4 Å) compared to that of III-V materials presents another major

¹Physics Department, Lancaster University, Lancaster LA1 4YB, UK. ²Department of Electrical Engineering and Electronics, University of Liverpool, Liverpool L69 7ZF, UK. ³Department of Physics, University of Warwick, Coventry CV4 7AL, UK. ⁴Stephenson Institute for Renewable Energy, University of Liverpool, Liverpool L69 7ZF, UK. ⁵Key Laboratory of Optoelectronic Chemical Materials and Devices, Jiangnan University, Wuhan 430056, China. ⁶Institute of Fundamental and Frontier Sciences, University of Electronic Science and Technology of China, Chengdu 610054, China. [†]Present address: Department of Science Education, Federal University of Agriculture, Makurdi, PMB 2373, Nigeria. Correspondence and requests for materials should be addressed to E.A.A. (email: ezeanyabe@hotmail.co.uk) or Y.C.C. (email: caosome@126.com) or Q.D.Z. (email: q.zhuang@lancaster.ac.uk)

obstacle to overcome. Unlike the growth of II-VI NWs such as ZnO on graphene^{10,16–18} and graphitic substrates¹⁹ which has been extensively investigated with optimized conditions, the growth of III-V semiconductor NWs on GS is currently in its formative stage and requires extensive studies for growth optimization⁵. However, compared to the traditional III-V substrates, graphite (like all other carbon related materials) is highly conductive thermally^{20,21} and temperature-sensitive^{22,23}. These features imply a significant modification to the adatom kinetics during epitaxy in particular, a high rate of re-evaporation²⁴ which would result in a low yield of NWs ensembles. Moreover, it has been demonstrated¹⁰ that the surface morphology and density of ZnO nanostructures on graphene are strongly temperature dependent. Although InAs NWs are more sensitive to growth conditions when compared to other III-V materials²⁵, the growth parameter study and the control of InAs NWs morphology and distribution on GS is still lacking. It is well established that the size and distribution of NWs can be controllably manipulated using basic growth parameters^{26,27}. Hence, an investigation of the influence of growth parameters and the conditions for realizing optimal InAs NWs with controlled geometry is crucial. Furthermore, most III-V semiconductor NWs are plagued by the presence of wurtzite (WZ) and zinc-blende (ZB) crystal phase mixtures (polytypism)^{28–30} which function as traps for carriers,³¹ reduce carrier mobility³² and conductivity³³. Polytypism also results in electron scattering at stacking faults or twin planes^{34,35} which is detrimental to their optical properties and device applications. As a result, to exploit the potential of NWs/GS, it is crucial to investigate the conditions for realizing InAs NWs/graphite structures with controllable geometry and low defect density. The few available reports of self-catalyzed^{36–38} and Au-assisted¹⁵ InAs NWs growth by metal-organic chemical vapor deposition (MOCVD) and GaAs³⁹ NWs growth by molecular beam epitaxy (MBE) on GS have been limited to basic NWs synthesis. Additionally, the yield of vertically-aligned InAs NWs is relatively low $\sim [(2-7) \times 10^8 \text{ cm}^{-2}]$ and requires more extensive studies for growth optimization⁵. In a previous study, we reported the growth of vertically aligned InAs NWs on graphite with highly uniform diameters through optimized In droplets²⁸. The growth of high quality, nontapered and ultrahigh aspect ratio InAs_{1-x}Sb_x NWs was also demonstrated on graphite²⁹. It was shown that NW nucleation and growth is facilitated by the predeposited In droplets. The In-assisted growth of InAs and InAsSb NWs on Si substrates was also demonstrated^{40–42}. In this paper, we seek to demonstrate the control of morphology and spatial distribution of InAs NWs as a function of growth parameters including growth temperature (T_G), growth rate (ξ) and V/III flux ratio (Ψ) with the aim of growth optimization. In particular, we intend to obtain a high yield of vertically-aligned InAs NWs with high aspect ratio and superior crystal structure for functional device applications. It is demonstrated that the self-catalyzed growth of InAs NWs with significantly improved morphology can be achieved within a relatively narrow temperature window and restricted domain of growth rate and V/III flux ratio. In comparison to previous reports of self catalyzed InAs NWs, a significantly reduced density of defects was observed in as-grown nanowires.

Results and Discussion

Optimization of InAs Nanowire Growth. The scanning electron microscope (SEM) images in Fig. 1 shows the dependence of InAs NWs density and morphology on growth temperature (T_G) in sample series A. The NWs exhibit a homogeneous diameter along their entire length without any measurable tapering. At the lowest temperature (400 °C), a dominant cluster (islands) growth was observed. A slight increase in T_G to 420 °C yielded a sparse NW distribution ($\sim 5.28 \times 10^8 \text{ cm}^{-2}$), and a maximum yield of $\sim 8.09 \times 10^8 \text{ cm}^{-2}$ was obtained for a further increase in temperature to 435 °C (Fig. 1b). Increasing T_G into the 450–475 °C range led to a decrease in NW density as shown in Fig. 1(c,d). The observed dependence of NW density on T_G can be explained by the kinetic modifications to the distribution of pre-deposited In droplets³⁰. A kinetically inhibited adatom mobility at a low temperature (400 °C) promotes the development of small but highly dense droplets leading to the growth of surface clusters at the expense of NWs. An increase in T_G in the range of 420–435 °C results in the formation of slightly large but well separated droplets which favour the growth of high density of NWs. It is therefore not surprising that the highest yield of vertically-aligned NWs was obtained at 435 °C. However, for higher temperatures ($435 \text{ °C} < T_G \leq 475 \text{ °C}$), the nucleation droplets merge to form clusters and are consumed at the early stages of NW growth. In addition, the desorption rate of the droplets is significantly increased leading to less nucleation of NWs⁴³. Figure 2(a) shows the variation of NWs length (L_{NW}) as a function of T_G . Over 70% of measurable NWs in each sample were analyzed for each point. Gaussian approximations were then used for the determination of the error bars of the NWs geometry (L_{NW} and D_{NW}) which is expressed as the deviation from the mean geometry of normally distributed NWs. It can be seen that L_{NW} increases for a T_G increase in the range of 400–435 °C while it decreases in the temperature range of $435 \text{ °C} < T_G \leq 475 \text{ °C}$. Maximum L_{NW} was thus obtained at a T_G of 435 °C which is consistent with a previous report⁴⁴. It is worth noting that the dependence of L_{NW} on T_G is accompanied by an inverse dependence of diameter (D_{NW}) on T_G , e.g. the D_{NW} decreases first (up to 435 °C) then increases with a further rise in T_G . Consequently, long and thin NWs with a high aspect ratio (~ 83) was obtained at an optimal temperature of 435 °C (length and diameter of $2.58 \pm 0.34 \mu\text{m}$ and $\sim 31.21 \pm 6.59 \text{ nm}$ respectively). This also corresponds to the temperature which yields a high density of NWs. Notably, despite the high aspect ratio, the NWs remain vertically well-aligned without the presence of randomly oriented NWs. This demonstrates the feasibility of fabricating InAs NWs with good geometry which would allow for fundamental studies such as size-dependent quantum confinement effects. The observed phenomenon can be interpreted in terms of the diffusion-limited growth of NWs in MBE. It has been theoretically and experimentally shown that the axial growth of NWs by MBE is strongly dependent on adatom diffusion from the substrate to the droplet^{45,46}.

Consequently, at a low T_G of 400 °C, adatom diffusion is kinetically impeded and axial NW growth is suppressed in favour of cluster growth. A slight rise in T_G to 420 °C favours the diffusion of adatom towards the top of the NWs with considerable deposition on the sidewalls leading to the emergence of short and thick NWs. An increase in T_G to 430 °C further enhances the diffusion flux of adatoms with minimal deposition along the sidewalls. This translates to a surge in L_{NW} with a corresponding shrinkage in D_{NW} ^{24,47,48}. However, for the upper temperature limit ($T_G > 435 \text{ °C}$), adatom incorporation probability and diffusion flux is significantly reduced

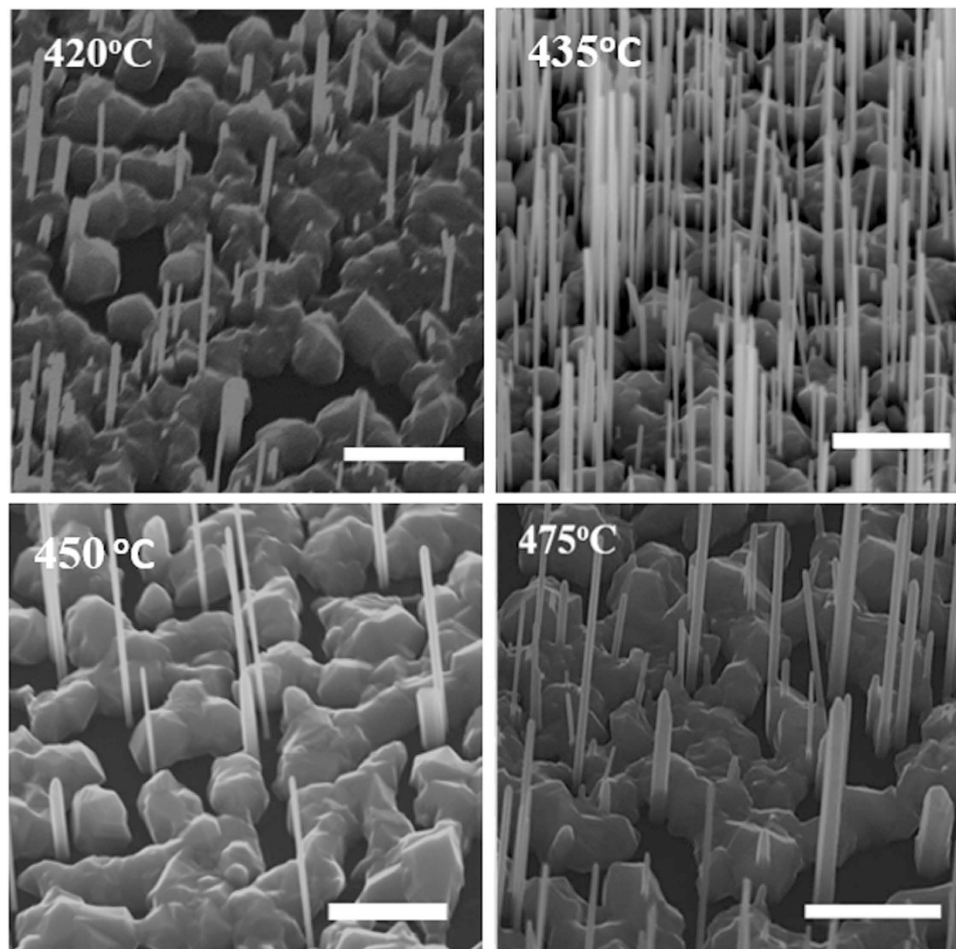


Figure 1. 45° tilted SEM images of InAs nanowires grown on graphitic substrates with a fixed In-flux at various temperatures in the range of 400–475 °C. The scale bars correspond to 1 μm.

due to unfavourable chemical potential gradient⁴⁹ and re-evaporation²⁴. Generally, NW growth was realized on graphite within the temperature domain of 400–475 °C which falls within the MBE growth window of InAs NWs (400–500 °C)^{2,44,50}.

Turning to sample series B, there was a clear and monotonic increase in NWs density with increasing growth rate (ξ) (Fig. 3, top panel). A high yield ($6.44 \times 10^8 \text{ cm}^{-2}$) of vertically-aligned NWs was obtained at a relatively high ξ of 0.3 ML/s. The increase in NW density with increasing ξ is associated with the dependence of NWs nucleation on In-flux. Higher In-flux results in the formation of a high density of In droplets due to the reduction in adatom diffusion time³⁰. This translates to an increase in NWs density as a function of ξ . This observation implies the availability of high NW growth rate which is favourable for realizing cost-effective devices. Intriguingly, the average L_{NW} slightly decreases with increasing ξ while D_{NW} remains nearly constant (Fig. 2b) leading to a slight decrease in NW aspect ratio with an increase in ξ . The observed decline in axial growth rate is understandable given the sharp rise in NWs density at constant supply of precursor flux which implies a reduction in the available growth species due to its consumption during NWs nucleation. In addition, the increase in ξ favours an increase in adatoms surface coverage with a suppression of adatom surface mobility. This results in a decreased diffusion flux of the adatoms from the substrate surface to the growth interface leading to a reduction in L_{NW} .

The influence of V/III flux ratio (Ψ) on InAs NWs growth in sample series C is depicted in Fig. 3 (Bottom panel). It reveals that NW nucleation is strongly dependent on Ψ , whereas no NW growth was realized at a relatively low Ψ of 27, an increase in Ψ to 51 resulted in a few NWs ($2.55 \times 10^7 \text{ cm}^{-2}$). The NW nucleation probability was enhanced by utilizing a highly As-rich conditions ($\Psi = 55$) evidenced by the increase in NWs yield. This demonstrates that an As-rich condition ($\Psi \geq 51$) is required for suppressing the growth of clusters in favour of vertically-aligned InAs NWs. The dependence of NW aspect ratio on Ψ in Fig. 2c also suggests that the axial NWs growth is promoted by As-rich conditions. Although there was no significant change in L_{NW} for a slight increase in Ψ to 55, it enabled the growth of thin NWs.

Structural property of as grown Nanowires. To gain insight into the crystal structures of as-grown NWs, high resolution transmission electron microscope (HRTEM) experiments were performed. However, in order to quantify the distribution of defects present in the NWs, a clear distinction between stacking faults (SFs)

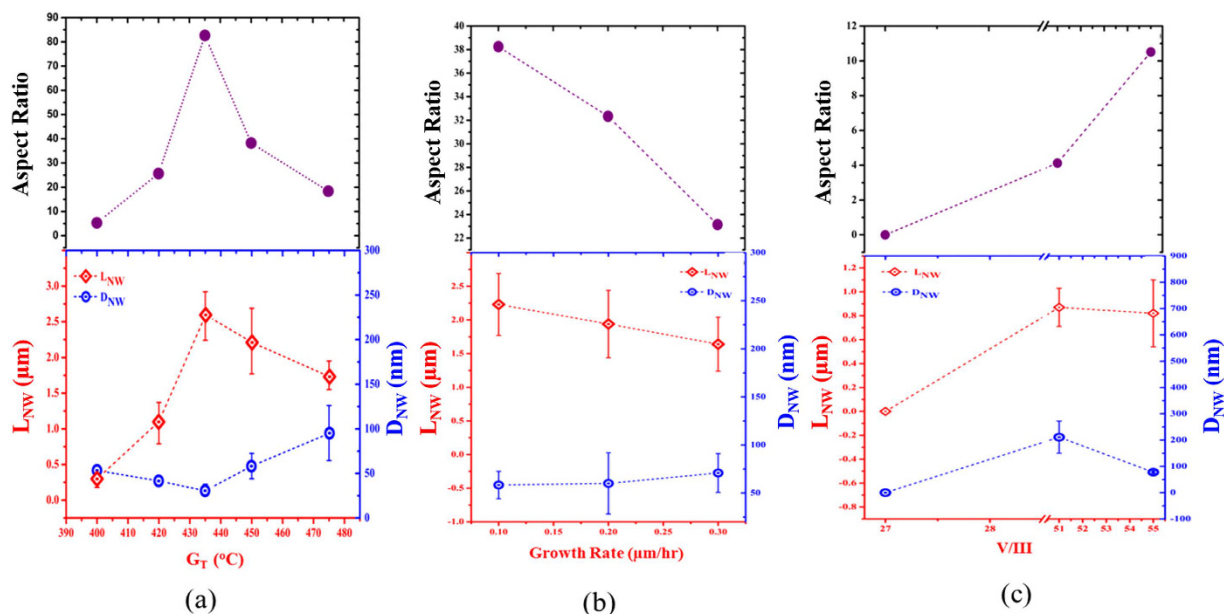


Figure 2. Aspect ratio (top), length (L_{NW}) and diameter (D_{NW}) (bottom) of InAs nanowires grown on graphitic substrate as a function of varied growth temperature (T_G) (a); growth rate (b) and V/III flux ratio (c).

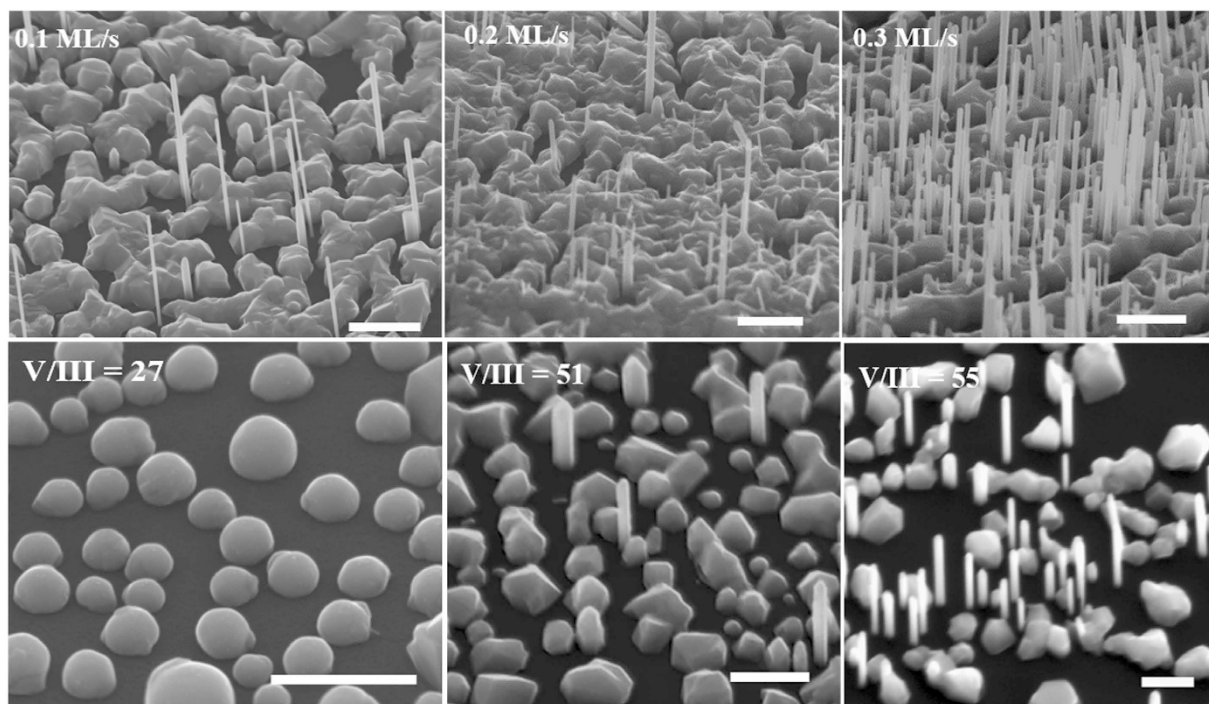


Figure 3. 45° tilted SEM images of InAs NWs grown on graphite at a constant growth temperature and As-flux but different growth rates (top panel) and V/III flux ratios (bottom panel). The scale bars for varied growth rates and V/III flux ratio images corresponds to 1 μm and 500 nm respectively.

and rotational twins (RTs) is made. A III-V semiconductor bilayer (BL) is composed of a pair of atomic layers with vertically stacked group III and group V atoms. The crystal structure of a semiconductor is dictated by the sequential arrangement of the BLs. A typical Zinc Blende (ZB) sequence is ...ABCABC... while a Wurtzite (WZ) sequence is ...ABABAB... where each letter represents a bilayer. A SF results from a partial distortion of the vertical stacking sequence either by the absence of a segment in the normal sequence or the inclusion of a single segment of the other crystal structure. In the ZB phase, a sequence of ABC $\overline{\text{A}}$ BABC indicates a SF with the fault line between C and A leading to the inclusion of a WZ unit ($\overline{\text{A}}\text{B}$) between the ZB segments. Similarly, for a WZ

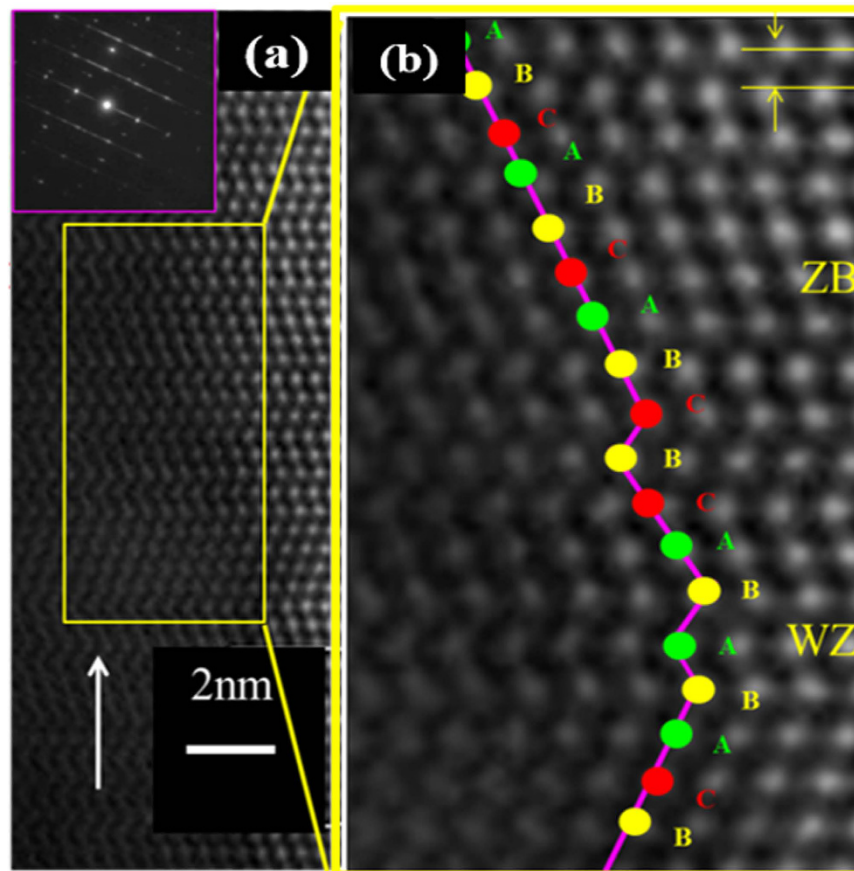


Figure 4. Typical HR-TEM image of InAs nanowires grown on graphite [the inset shows the selective area electron diffraction pattern] (a); an enlarged section of the HRTEM image (b).

phase a SF exists in a stacking sequence of the form $ABACBAB$ due to the inclusion of C which alters the regular WZ sequence. On the other hand a RT is created when a segment of a crystal is rotated by 60° around the growth axis ($\langle 111 \rangle$) such that it is translated to a mirror image of the regular segment. The interface between the regular and mirror segments is referred to as the twin boundary. A stacking sequence of $ABABCBABA$ for WZ phase and $ABCACBA$ for the ZB phase illustrates the presence of RTs. A representative high resolution TEM micrograph (Fig. 4a) shows the NWs/GS exhibits a ZB/WZ crystal phase mixture consistent with previous reports of self-assisted InAs NWs^{1,2,51}. An enlarged segment of the HRTEM image (Fig. 4b) clearly demonstrates the transition between the ZB and WZ phases with SF present. This polytype behaviour of III–V NWs has become the rule rather than the exception^{35,52,53} and has been mostly associated with the lower surface energy of the WZ phase in comparison to the corresponding crystalline orientation of the ZB material. As a consequence the WZ phase is more stable in NW structures with high surface to volume ratio^{27,54}. Classical nucleation theory has also been used to explain this phenomenon and attributed it to the lower WZ nucleation barrier compared to that of ZB^{55–57}. The electron diffraction pattern (inset of Fig. 4(a)) further confirms the mixed ZB/WZ crystal structure with multiple SFs on the $(111)/(0001)$ plane evidenced by the observable streaks in the diffraction pattern. An interplanar d-spacing of ~ 0.35 nm along the growth direction was obtained for the ZB segment (Fig. 4b) which corresponds to that of bulk ZB InAs (0.35 nm). Compared to our previous report³⁰ of InAs NWs, a significantly lower density of defects (SFs and RTs) was observed in the InAs/GS samples. A typically InAs NWs/Graphite contains about 225.35 ± 56.34 SFs per μm . We attribute this improvement to the well optimized growth conditions. Similarly, no dislocations were observed in the NWs which can be associated with the van der Waals epitaxy (vdWE) growth technique. One of the key advantages of vdWE is the absence of interfacial lattice mismatch induced strain^{58,59} owing to the circumvention of lattice-matching requirements. In addition, there is a near coherent in-plane lattice matching (0.49%) between InAs and the graphene honeycomb lattice. The distance of 4.263 Å for the graphene honeycomb-honeycomb along $(\bar{1}210)$ closely matches that of 4.284 Å for the nearest As-As or In-In bonds of ZB InAs^{37–39}.

Hybrid InAs/Graphite Infrared Photovoltaic Detectors. To investigate the electrical properties of as-grown NWs, InAs/Graphite infrared photovoltaic detectors with various mesa diameters of 25–200 μm were fabricated (see Method for device processing). Each mesa contains InAs NW ensembles with an estimated number of over 3000 based on the areal density. The bandgap diagram of the device^{60–62} in thermal equilibrium is shown in Fig. 5(a). The work function of Graphite is around 4.3–4.7 eV^{6,9,63–65}, while the Fermi level (E_F) of

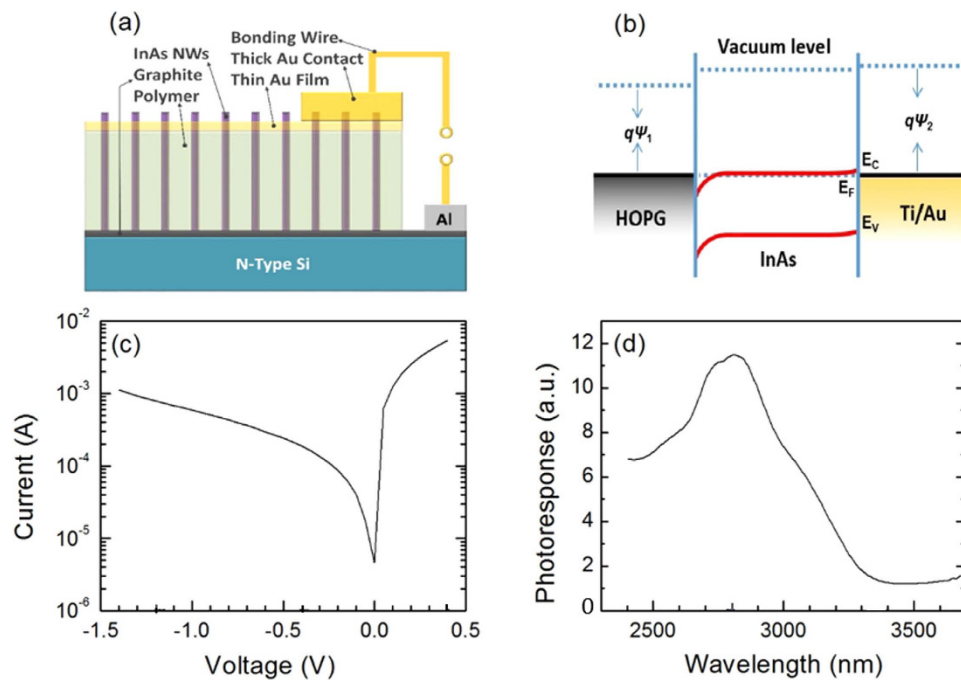


Figure 5. Schematic diagram of the NWs ensemble photodetector (a), bandgap diagram of InAs/Graphite heterojunction (b), I-V curve of a InAs NW ensemble/graphite hybrid device (c), and the room temperature spectral photoresponse of the hybrid device (d). The device mesa has a diameter of 25 μm .

InAs is $\sim 5.0 \text{ eV}$ ^{60,63}. This perspective leads to a downward band bending at the interface of InAs/Graphite which forms a depletion region for the holes. Such a depletion region would enable photodetection. A typical I-V profile of such device is shown in Fig. 5(b). It exhibits an asymmetric rectifying behaviour as expected from InAs/Graphite interface. The spectral photoresponse under the exiting wavelength of 2.4–3.7 μm is shown in Fig. 5(c). A photoresponse with a cut-off wavelength of 3.4 μm clearly implies photodetection from InAs NWs/graphite hybrid junction. The main peak located around 2.7 μm enables the device to work under part of near-infrared and mid-infrared bands.

Conclusion

In conclusion, the optimal conditions for the MBE growth of InAs NWs on graphite is explicated. It has been discovered that the NWs geometry and areal density are sensitive to the growth parameters of temperature, growth rate and V/II flux ratio. The areal density and length of InAs NWs increases as the growth temperature is increased from 400 to 435 $^{\circ}\text{C}$, a further increase induces a decrease in both, while a reversed dependence of diameter was observed within the same temperature regime. NWs on GS with high aspect ratio can be realized within a narrow temperature window of 420–450 $^{\circ}\text{C}$. As-rich conditions were found to promote NWs growth. In addition, the GS favours high growth rate of InAs NWs which is promising from a device perspective. Our study also reveals that the NWs exhibit significantly reduced defect density which is attributable to the well optimized growth conditions. This study enables the controllable epitaxy of high quality InAs NWs on GS which paves the way for the integration of InAs NWs with graphite for the fabrication of advanced functional devices.

Methods

InAs Nanowire Synthesis on Graphite. The InAs NWs were grown on GS by solid-source MBE. Mechanically exfoliated graphite films from highly oriented pyrolytic graphite (HOPG) were transferred onto Si (111) substrates and subsequently loaded into the system and thermally outgassed. Indium (In) droplets were pre-deposited on the films prior to growth initiation at pre-optimised conditions (In-flux of 2.2×10^{-7} mbar and deposition temperature of 220 $^{\circ}\text{C}$). The size of the droplet was about 70 nm with a number density of $6.33 \times 10^8 \text{ cm}^{-2}$. Three series of samples (A–C) were grown as a function of T_G , ξ and Ψ respectively. Firstly, in order to identify the effect of growth temperature, T_G was varied in the range of 400–475 $^{\circ}\text{C}$ at a fixed ξ and Ψ of ~ 55 for a growth duration of 60 min in sample series A. Then, the samples of series B were grown at various growth rates ranging from 0.1 to 0.3 ML/s at a fixed Ψ and constant T_G of 450 $^{\circ}\text{C}$, to investigate the dependence of InAs NWs growth on ξ . Finally, the samples of series C were grown at a fixed T_G (450 $^{\circ}\text{C}$) and In-flux with varying Ψ in the range of 27–55 to study the influence of Ψ on NW growth. For all the samples, the NWs growth was initiated and terminated by simultaneously introducing and shutting of both In and As supplies.

Microscopy. The surface morphology of the NWs was investigated using a FEI XL30 SFEG scanning electron microscope (SEM). Transmission electron microscope (TEM) images were taken with a JEOL-JEM 2100 microscope working at 200 kV.

Device Fabrication. The devices were processed using standard photolithography. A layer of SU8 with a thickness of around 4 μm was deposited via spin coating and UV exposure to encapsulate the nanowires. The SU8 was then thinned via reactive ion etching using a mixture of O_2 and SF_6 (35/5 sccm's respectively) to free the tips of the nanowires. Circular devices with varying diameters (25–200 μm) were defined by a thin (~ 10 nm) gold layer which was deposited on and between the exposed tips of nanowires. To allow electrical connection to these devices a thicker top contact layer of Ti/Au (20/200 nm) was defined over some specific part of the device area for Ohmic contact. A back Ohmic contact of Aluminium with a thickness of about 200 nm was finally deposited on the reverse of the substrate to form a complete current loop.

Device Testing. The electrical Current-Voltage (I-V) profile of the devices was measured with a Keithley Source Measure Unit. The spectral response was determined using phase sensitive detection comprising a lock-in-amplifier, and an iHR320 monochromator with a blaze grating wavelength of 2 μm was used in conjunction with a global light source.

References

- Wei, W. *et al.* Direct Heteroepitaxy of Vertical InAs Nanowires on Si Substrates for Broad Band Photovoltaics and Photodetection. *Nano Lett.* **9**, 2926–2934 (2009).
- Dimakis, E. *et al.* Self-Assisted Nucleation and Vapor–Solid Growth of InAs Nanowires on Bare Si(111). *Cryst. growth Des.* **11**, 4001–4008 (2011).
- Wallart, X., Lastennet, J., Vignaud, D. & Mollot, F. Performances and limitations of InAs/InAlAs metamorphic heterostructures on InP for high mobility devices. *Appl. Phys. Lett.* **87**, 43504 (2005).
- Ihn, S.-G. & Song, J.-I. InAs nanowires on Si substrates grown by solid source molecular beam epitaxy. *Nanotechnology* **18**, 355603 (2007).
- Munshi, A. M. & Weman, H. Advances in semiconductor nanowire growth on graphene. *Phys. Status Solidi-Rapid Res. Lett.* **7**, 713–726 (2013).
- Bae, S. *et al.* Roll-to-roll production of 30-inch graphene films for transparent electrodes. *Nat. Nanotechnol.* **5**, 574–578 (2010).
- Wassei, J. K. & Kaner, R. B. Graphene, a promising transparent conductor. *Mater. Today* **13**, 52–59 (2010).
- De-Arco, L. G. *et al.* Continuous, Highly Flexible, and Transparent Graphene Films by Chemical Vapor Deposition for Organic Photovoltaics. *Nano Lett.* **4**, 2865–2873 (2010).
- Li, X. *et al.* Large-Area Synthesis of High-Quality and Uniform Graphene Films on Copper Foils. *Science* **324**, 1312–1314 (2009).
- Kim, Y. J., Lee, J. H. & Yi, G. C. Vertically aligned ZnO nanostructures grown on graphene layers. *Appl. Phys. Lett.* **95**, 213101–213103 (2009).
- Park, H. *et al.* Graphene Cathode-Based ZnO Nanowire Hybrid Solar Cells. *Nano Lett.* **13**, 233–239 (2013).
- Alper, J. P., Gutes, A., Carraro, C. & Maboudian, R. Semiconductor nanowires directly grown on graphene - towards wafer scale transferable nanowire arrays with improved electrical contact. *Nanoscale* **5**, 4114–4118 (2013).
- Miao, X. *et al.* High Efficiency Graphene Solar Cells by Chemical Doping. *Nano Lett.* **12**, 2745–2750 (2012).
- Lee, C. *et al.* Flexible Inorganic Nanostructure Light-Emitting Diodes Fabricated on Graphene Films. *Adv. Mater.* **23**, 4614–4619 (2011).
- Wallentin, J., Kriegner, D., Stangl, J. & Borgström, M. T. Au-Seeded Growth of Vertical and in-Plane III–V Nanowires on Graphite Substrates. *Nano Lett.* **14**, 1707–1713 (2014).
- Kumar, B. *et al.* Controlled Growth of Semiconducting Nanowire, Nanowall, and Hybrid Nanostructures on Graphene for Piezoelectric Nanogenerators. *ACS Nano* **5**, 4197–4204 (2011).
- Kim, Y. J. *et al.* Hydrothermally grown ZnO nanostructures on few-layer graphene sheets. *Nanotechnology* **22** (2011).
- Park, W. I., Lee, C. H., Lee, J. M., Kim, N. J. & Yi, G. C. Inorganic nanostructures grown on graphene layers. *Nanoscale* **3**, 3522–3533 (2011).
- Ng, H. T. *et al.* Growth of epitaxial nanowires at the junctions of nanowalls. *Science* **300**, 1249 (2003).
- Klemens, P. G. & Pedraza, D. F. Thermal conductivity of graphite in the basal plane. *Carbon N. Y.* **32**, 735–741 (1994).
- Vlassiuk, I. *et al.* Electrical and thermal conductivity of low temperature cvd graphene: the effect of disorder. *Electr. Therm. Conduct. low Temp. CVD graphene Eff. Disord.* **22**, 275716 (2011).
- Huong, P., Cavagnat, R., Ajayan, P. & Stephan, O. Temperature- dependent vibrational spectra of carbon nanotubes. *Phys. Rev. B* **51**, 10048–10051 (1995).
- Tan, P. H., Deng, Y. M. & Zhao, Q. Temperature- dependent Raman spectra and anomalous Raman phenomenon of highly oriented pyrolytic graphite. *Phys. Rev. B* **58**, 5435–5439 (1998).
- Dubrovskii, V. G., Sibirev, N. V., Cirilin, G. E., Harmand, J. C. & Ustinov, V. M. Theoretical analysis of the vapor-liquid-solid mechanism of nanowire growth during molecular beam epitaxy. *Phys. Rev. E* **73**, 21603–21610 (2006).
- Dick, K. A., Deppert, K., Samuelson, L. & Seifert, W. Optimization of Au- assisted InAs nanowires grown by MOVPE. *J. Cryst. Growth* **297**, 326–333 (2006).
- Joyce, H. J., Wong-Leung, J., Gao, Q., Tan, H. H. & Jagadish, C. Phase perfection in zinc Blende and Wurtzite III- V nanowires using basic growth parameters. *Nano Lett.* **10**, 908–915 (2010).
- Dick, K. A. *et al.* Control of III–V nanowire crystal structure by growth parameter tuning. *Semicond. Sci. Technol.* **25**, 24009 (2010).
- Zhuang, Q. *et al.* Graphitic platform for self-catalysed InAs nanowires growth by molecular beam epitaxy. *Nanoscale Res. Lett.* **9**, 321–327 (2014).
- Zhuang, Q. D. *et al.* Sb-Induced Phase Control of InAsSb Nanowires Grown by Molecular Beam Epitaxy. *Nano Lett.* **15**, 1109–1116 (2015).
- Anyebe, E. A. *et al.* Self-catalysed growth of InAs nanowires on bare Si substrates by droplet epitaxy. *Rapid Res. Lett.* **8**, 658–662 (2014).
- Wallentin, J., Ek, M., Wallenberg, L. R., Samuelson, L. & Borgström, M. T. Electron Trapping in InP Nanowire FETs with Stacking Faults. *Nano Lett.* **12**, 151–155 (2011).
- Schroer, M. D. & Petta, J. R. Correlating the Nanostructure and Electronic Properties of InAs Nanowires. *Nano Lett.* **10**, 1618–1622 (2010).
- Thelander, C., Caroff, P., Plissard, S., Dey, A. W. & Dick, K. A. Effects of Crystal Phase Mixing on the Electrical Properties of InAs Nanowires. *Nano Lett.* **11**, 2424–2429 (2011).
- Stiles, M. D. Electron transmission through silicon stacking faults. *Phys. Rev.* **41**, 5280–5282 (1990).
- Caroff, P. *et al.* Controlled polytypic and twin-plane superlattices in III- V nanowires. *Nat. Nanotechnol.* **4**, 50–55 (2009).
- Mohseni, P. K. *et al.* InxGa1-xAs Nanowire Growth on Graphene: van der Waals Epitaxy Induced Phase Segregation. *Nano Lett.* **13**, 1153–1161 (2013).

37. Hong, Y. J. & Fukui, T. Controlled van der Waals Heteroepitaxy of InAs Nanowires on Carbon Honeycomb Lattices. *Nano. Lett.* **5**, 7576–7584 (2011).
38. Hong, Y. J., Lee, W. H., Wu, Y., Ruoff, R. S. & Fukui, T. van der Waals Epitaxy of InAs Nanowires Vertically Aligned on Single-Layer Graphene. *Nano. Lett.* **12**, 1431–1436 (2012).
39. Munshi, A. M. *et al.* Vertically Aligned GaAs Nanowires on Graphite and Few-Layer Graphene: Generic Model and Epitaxial Growth. *Nano Lett.* **12**, 4570–4576 (2012).
40. Anyebe, E. A. *et al.* Surfactant effect of antimony addition to the morphology of self-catalyzed InAs_{1-x}Sb_x nanowires. *Nano Res.* **8**, 1309–1319 (2015).
41. Anyebe, E. A. *et al.* Realization of vertically aligned, ultra-high aspect ratio InAs_{1-x}Sb_x nanowires on graphitic substrates. *Nano. Lett.* **15**, 4348–4355 (2014).
42. Anyebe, E. A. & Zhuang, Q. Self-catalysed InAs_{1-x}Sb_x nanowires grown directly on bare Si substrates. *Mater. Res. Bull.* **60**, 572–575 (2014).
43. Mandl, B. *et al.* Growth Mechanism of Self-Catalyzed Group III-V Nanowires. *Nano Lett.* **10**, 4443–4449 (2010).
44. Koblmüller, G. *et al.* Self-induced growth of vertical free-standing InAs nanowires on Si (111) by molecular beam epitaxy. *Nanotechnology* **21**, 365602 (2010).
45. Dubrovskii, V. G., Sibirev, N. V., Harmand, J. C. & Glas, F. Growth kinetics and crystal structure of semiconductor nanowires. *Phys. Rev. B* **78**, 235301–235310 (2008).
46. Dubrovskii, V. G. *et al.* Diffusion-induced growth of GaAs nanowhiskers during molecular beam epitaxy: Theory and experiment. *Phys. Rev. B* **71**, 205325 (2005).
47. Mohammad, S. N. Substrate-mediated diffusion-induced growth of single-crystal nanowires. *J. Chem. Phys.* **131**, 204703 (2009).
48. Harmand, J. C. *et al.* GaAs nanowires formed by Au-assisted molecular beam epitaxy: Effect of growth temperature. *J. Cryst. Growth* **301**, 853–856 (2007).
49. Tchernycheva, M. *et al.* Au-assisted molecular beam epitaxy of InAs nanowires: Growth and theoretical analysis. *J. Appl. Phys.* **102**, 94313–94318 (2007).
50. Hertenberger, S. *et al.* Rate-limiting mechanisms in high-temperature growth of catalyst-free InAs nanowires with large thermal stability. *Nanotechnology* **23**, 235602 (2012).
51. Jing, Y. *et al.* Catalyst-free Heteroepitaxial MOCVD Growth of InAs Nanowires on Si Substrates. *J. Phys. Chem. C* **118**, 1696–1705 (2014).
52. Lehmann, S., Wallentin, J., Jacobsson, D., Deppert, K. & Dick, K. A. A General Approach for Sharp Crystal Phase Switching in InAs, GaAs, InP, and GaP Nanowires. Using Only Group V Flow. *Nano Lett.* **13**, 4099–4105 (2013).
53. Caroff, P., Bolinsson, J. & Johansson, J. Crystal Phases in III-V Nanowires: From Random Toward Engineered Polytypism. *IEEE J. Sel. Top. Quantum Electron.* **17**, 829–846 (2011).
54. Johansson, J. *et al.* Diameter dependence of the wurtzite–zinc blende transition in InAs nanowires. *J. Phys. Chem. C* **114**, 3837–3842 (2010).
55. Glas, F., Harmand, J. C. & Patriarche, G. Why does wurtzite form in nanowires of III-V zinc blende semiconductors? *Phys. Rev. Lett.* **99**, 146101 (2007).
56. Johansson, J. *et al.* Effects of Supersaturation on the Crystal Structure of Gold Seeded III-V Nanowires. *Cryst. Growth Des.* **9**, 766–773 (2009).
57. Krogstrup, P. *et al.* Impact of the Liquid Phase Shape on the Structure of III-V Nanowires. *Phys. Rev. Lett.* **106**, 125504–125505 (2011).
58. Jaegermann, W., Rudolph, R., Klein, A. & Pettenkofer, C. Perspectives of the concept of van der Waals epitaxy: growth of lattice mismatched GaSe(0001) films on Si(111), Si(110) and Si(100). *Thin Solid Films* **380**, 276–281 (2000).
59. Utama, M. I. B. *et al.* Recent developments and future directions in the growth of nanostructures by van der Waals epitaxy. *Nanoscale* **5**, 3570–3588 (2013).
60. Miao, J. *et al.* Single InAs nanowire room-temperature near-infrared photodetectors. *ACS Nano* **8**, 3628–3635 (2014).
61. Miao, J. *et al.* High-responsivity graphene/InAs nanowire heterojunction near-infrared photodetectors with distinct photocurrent on/off ratios. *Small* **11**, 936–942 (2015).
62. Di Bartolomeo, A. Graphene Schottky diodes: An experimental review of the rectifying graphene/semiconductor heterojunction. *Physics Reports* **606**, 1–58 (2016).
63. Czerw, R. *et al.* Substrate-interface interactions between carbon nanotubes and the supporting substrate. *Phys. Rev. B* **66**, 33408 (2002).
64. Huang, J. H., Fang, J. H., Liu, C. C. & Chu, C. W. Effective work function modulation of graphene/carbon nanotube composite films as transparent cathodes for organic optoelectronics. *ACS Nano* **5**, 6262–6271 (2011).
65. Jo, G. *et al.* Tuning of a graphene-electrode work function to enhance the efficiency of organic bulk heterojunction photovoltaic cells with an inverted structure. *Appl. Phys. Lett.* **97**, 213301 (2010).

Acknowledgements

We are grateful to EPSRC Lancaster Impact Acceleration Account, Oxford Instrument and Gas Sensing Solutions for their financial support. E. A. Anyebe would like to thank TETFund Nigeria for their support. Dr. Cao thanks the funds from Basic Research Project of Wuhan City (2015011701011593) and 4th Yellow Crane Talent Programme of Wuhan City (08010004).

Author Contributions

Q.D.Z. Y.C.C. and H.D.L. conceived and designed the experiments and led the research. E.A.A. conducted the MBE growth and wrote the major part of the paper. I.S. and Z.M.J. contributed in device processing, characterisation and writing the part of devices. A.M.S. performed HRTEM measurements. M.A.R. and T.D.V. conducted the SEM measurements. R.H. contributed to the set-up device characterisation apparatus.

Additional Information

Competing Interests: The authors declare no competing financial interests.

How to cite this article: Anyebe, E. A. *et al.* Optimization of self-catalyzed InAs Nanowires on flexible graphite for photovoltaic infrared photodetectors. *Sci. Rep.* **7**, 46110; doi: 10.1038/srep46110 (2017).

Publisher's note: Springer Nature remains neutral with regard to jurisdictional claims in published maps and institutional affiliations.



This work is licensed under a Creative Commons Attribution 4.0 International License. The images or other third party material in this article are included in the article's Creative Commons license, unless indicated otherwise in the credit line; if the material is not included under the Creative Commons license, users will need to obtain permission from the license holder to reproduce the material. To view a copy of this license, visit <http://creativecommons.org/licenses/by/4.0/>

© The Author(s) 2017